Check for updates

ChemSusChem

Research Article
doi.org/10.1002/cssc.202402706

Chemistry Europe
European Chemical Societies Publishing

www.chemsuschem.org

Ionic Conductive Binder Based on Fast Ion Conductor Interface Compatibilization for Lithium–Sulfur Batteries

Lou Da, Xiao Fangrong, Hua Lan, Li Xufeng, Wang Wenqiang,* and Wang Gengchao*

Binders are the key components for maintaining the integrity of sulfur electrodes in lithium–sulfur batteries. However, the traditional insulating binders have a negative impact on the charge transfer within the electrodes, which is an important factor leading to the poor rate performance of lithium–sulfur batteries. Herein, an ionic conductive binder (LPABM-*d*-LATP) based on the interface compatibilization of fast ionic conductor is synthesized by in situ emulsion polymerization and lithiation neutralization. The modified $Li_{1.3}Al_{0.3}Ti_{1.7}(PO_4)_3$ nanoparticles with double bonds (*d*-LATP) are covalently bonded to the lithiated copolymer to form a core–shell structure, which enables LPABM-*d*-LATP binder to synergistically promote the migration of lithium ions, making the room-temperature ionic conductivity of LPABM-*d*-LATP reaches 2.5×10^{-4} S cm^{-1}. As a result, as-assembled lithium sulfur battery based on the LPABM-*d*-LATP binder displays a specific capacity of 941 m Ah g^{-1} at a high rate of 4 C and a capacity retention of 80.1% after 200 cycles at 0.5 C. This ionic conductive binder can make remarkable improvement in the excellent electrochemical performance of lithium–sulfur batteries.

1. Introduction

Advanced aircraft such as unmanned aerial vehicles or drones have distinctive and incomparable advantages in both conventional civilian and industrial applications; their market has experienced unprecedented prosperity in recent years.[1–3] As a crucial component in the advanced aircraft system, the development and progress of batteries have a direct impact. Among electrochemical energy storage devices such as lithium-ion batteries and lithium metal batteries,[4–6] lithium–sulfur batteries possess a remarkably high theoretical specific capacity (1675 m Ah g^{-1}) and energy density (2600 W h kg^{-1}).[7–9] Moreover, compared with metal oxides, sulfur as a cathode can significantly reduce costs and weight, achieving a relatively high gravimetric energy density,[10–12] which is of crucial significance for the performance of aircraft. However, the sulfur employed as a cathode material has several prevalently recognized issues: 1) a substantial volume variation (≈80%) between the sulfur and the discharge product lithium sulfide (Li_2S),[13] 2) the emergence of the "shuttle effect" attributable to the dissolution of lithium polysulfide (LiPS),[14] and 3) sluggish kinetics arising from its insulating properties with respect to electrons and lithium ions.[15,16] These formidable challenges collectively give rise to the suboptimal rate performance and rapid energy dissipation of lithium–sulfur batteries.[17,18] Consequently, it becomes imperative to enhance the utilization efficiency and rate performance of the active material by expediting the migration of charges.

Many strategies have been developed over the past decade to address the above problems, such as improvement of sulfur host materials,[19,20] replacement of electrolyte,[21,22] using decorated separator,[23,24] and utilization of multifunctional binders.[25–27] Among these strategies, multifunctional binders for lithium–sulfur batteries have the advantages of low design cost, easy operation and suitability for large-scale application, thus representing an extremely viable approach.[28,29] Regarding the functionality of binders, much attention has recently been paid to binders with conductive features that accelerate the transmission of electrons or ions during the charging/discharging process.[30,31] For example, Cheng et al. reported a binder consisting of sodium alginate cross-linked with $Ti_3C_2T_x$ (T = −OH, −O, −F, etc.), which showed better adhesion ability and electronic conductivity.[32] Our group previously reported a conductive binder based on the conductive polymer (poly(3,4-ethylenedioxythiophene)), which can effectively enhance the cycle stability and rate performance of lithium–sulfur batteries.[33] In addition to electronically conductive binders, ionic conductive binders can also effectively improve the conductivity of lithium–sulfur batteries by providing ionic conductive channels in lithium–sulfur batteries to promote Li^+ transport. For instance, Lin et al. reported a polymer binder based on polyethylene, which has a fast lithium migration and accelerates the reaction kinetics of lithium–sulfur batteries.[34] Compared with electron-conductive binders, ionic conductive binders have received relatively less research attention. This insufficient research has rendered ionic conduction a bottleneck issue for lithium–sulfur batteries. Therefore, new ionic conductive binders urgently need to be explored.

Herein, an ionic conductive binder (LPABM-*d*-LATP) formed via covalent bonds between a lithiated copolymer (LPABM) composed of acrylonitrile (AN), methacrylic acid (MAA), and butyl acrylate (BA) and the modified $Li_{1.3}Al_{0.3}Ti_{1.7}(PO_4)_3$, namely, LATP (*d*-LATP), is synthesized. LPABM-*d*-LATP is an organic–inorganic

L. Da, X. Fangrong, H. Lan, L. Xufeng, W. Wenqiang, W. Gengchao
Shanghai Engineering Research Center of Hierarchical Nanomaterials
Shanghai Key Laboratory of Advanced Polymeric Materials
School of Materials Science and Engineering
East China University of Science and Technology
Shanghai 200237, China
E-mail: wangwenqiang@ecust.edu.cn
gengchaow@ecust.edu.cn

Supporting information for this article is available on the WWW under https://doi.org/10.1002/cssc.202402706

composite emulsion with core–shell structure, in which the inorganic particles serve as the core and the copolymer with hydrophilic groups attached acts as the shell. When LATP is compounded with LPABM through covalent bonds, due to the synergistic effect of two components enhanced by the interfacial compatibilization, the high-efficient lithium-ion (Li^+) migration channels and an inorganic-reinforced skeleton with the multifunctional polysulfide-trapping ability derived from LPABM will be formed. Therefore, LPABM-*d*-LATP is expected to exhibit the following advantages when used as a binder for sulfur cathode materials: 1) the *d*-LATP-reinforced LPABM skeleton can efficiently bind active materials with sharp volume changes; 2) the high-efficient Li^+ migration channels constructed by the interface compatibilization of *d*-LATP and –COOLi endow the sulfur cathode with rapid Li^+ migration; and 3) LPABM rich in –COOR, –COOH, –COOLi, and –CN can trap intermediate LiPS. As a result, as-assembled lithium–sulfur battery based on LPABM-*d*-LATP binder showed an initial specific capacity of 1204 m Ah g^{-1} (defined by the mass of active material in cathode) at 0.1 C, a specific capacity of 941 m Ah g^{-1} at a high rate of 4 C, and a capacity retention of 80.1% after 200 cycles of a 0.5 C cycling test (with only 0.1% decay per cycle).

2. Results and Discussion

As shown in **Figure 1**a, a composite ionic conductive binder, denoted as LPABM- *d*-LATP, is prepared with the double bond-modified LATP and functional unsaturated monomers by emulsion polymerization and lithiation neutralization. To improve the dispersion uniformity of the LATP nanoparticles in the polymer matrix, chloro(dimethyl)vinylsilane was used as the coupling agent to achieve double-bond grafting on the surface of the LATP nanoparticles. The Fourier transform infrared spectroscopy (FTIR) spectra showed that there were obvious C—H stretching peaks (2925 and 2854 cm^{-1}) and the peak of ≈1630 cm^{-1} blueshift in the *d*-LATP, which proved that the vinyl groups were successfully grafted to the surface of the LATP nanoparticles (Figure S1, Supporting Information). Figure S2, Supporting Information, shows the change in contact angle before and after modifying LATP with silane coupling agent. After modification, the water contact angle increases from 23.0° to 40.5°. This indicates that the hydrophobicity of *d*-LATP is improved, which can improve its compatibility with the polymer matrix during emulsion polymerization. Therefore, the *d*-LATP easily participated in free radical polymerization with unsaturated monomers.

On the basis of the obtained *d*-LATP, it was introduced into a copolymerization system consisting of BA as a soft monomer, AN as a hard monomer, and MAA as a lithiable monomer to emulsion polymerization. Due to the large surface free energy and polymerization-active double bonds on the surface of LATP, the monomers will aggregate, adsorb to the surface, and polymerize to form composite emulsion particles (PABM-*d*-LATP) with in situ encapsulated copolymers (PABM). It is worth emphasizing that, due to the highly hydrophilic carboxyl groups present in MAA, the encapsulating layer of the copolymer may exhibit a tendency for the carboxyl groups to face the aqueous phase. Upon further neutralization by the introduction of LiOH, the carboxyl groups are transformed into negatively charged carboxylate ions, which are able to provide vacancies for lithium-ion hopping transport.

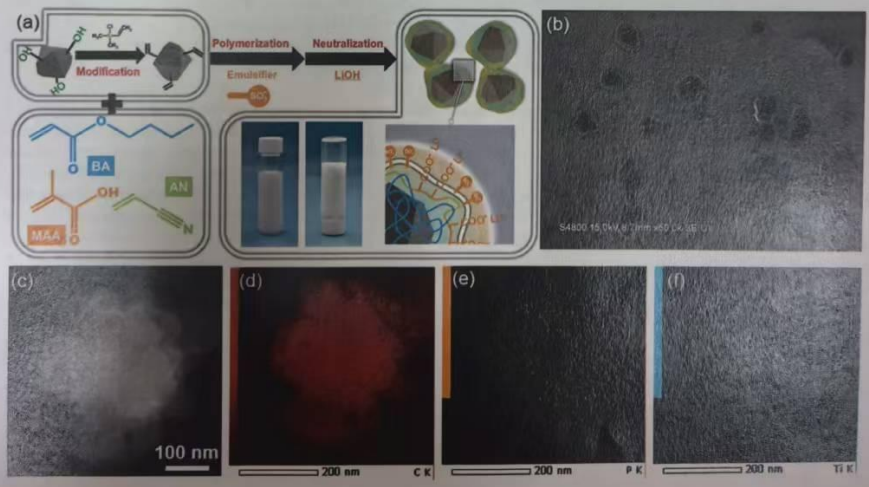

Figure 1. a) Schematic diagram of the synthesis process of LPABM-*d*-LATP ionic conductive composite emulsion. b) FE-SEM image of LPABM-*d*-LATP emulsion after standing for 24 h. c) TEM image and d–f) TEM–EDS elemental mappings of LPABM-*d*-LATP.

And after standing for another 24 h, there is no obvious settlement of inorganic fillers (as shown in the insets of Figure 1a). Figure 1b shows the scanning electron microscope (SEM) image of LPABM-*d*-LATP, from which it can be seen that the LPABM-*d*-LATP emulsion is well dispersed, and the size of the emulsion particles is between 200 and 300 nm. Before the in situ emulsion polymerization was carried out, the SEM image of LATP particles is shown in Figure S3, Supporting Information, which shows that the particles are irregular in shape and show obvious edges and corners. Compared with before polymerization, no separate inorganic filler component appeared after polymerization, indicating that the emulsion particles were encapsulated on the surface of the *d*-LATP particles. In contrast, if these two substances are simply mixed, an inhomogeneous mixture will be obtained (Figure S4, Supporting Information). These prove the success of in situ polymerization of LPABM on the surface of *d*-LATP. Meanwhile, the transmission electron microscopy (TEM) characterization of LPABM-*d*-LATP is carried out, as depicted in Figure 1c. When correlated with the energy-dispersive spectroscopy (EDS) mapping results shown in Figure 1d–f, it is distinctly evident that there exists a homogeneous distribution of carbon elements on the surface of this structure. Although the signal of phosphorus elements and titanium elements is relatively weak, it still exhibits a clear contour. These phenomena can be attributed to the fact that a copolymer layer coats the surface of *d*-LATP. Consequently, it can be inferred that LPABM-*d*-LATP possesses a microscopic structure featuring *d*-LATP as the core and the copolymer as the shell.

In addition, the chemical composition of LPABM-*d*-LATP and its components were further investigated by FTIR (**Figure 2**a and Figure S5, Supporting Information). It has a stretching vibration peak at 1740 cm^{-1} corresponding to the C═O in –COOR, a stretching vibration peak at 2230 cm^{-1} corresponding to the –CN in AN, a stretching vibration peak at 1450 cm^{-1} corresponding to the C═O in –COOH, and the disappearance of the stretching characteristic peaks of C═C in BA, AN, and MAA at 1635 cm^{-1}. Moreover, compared to the original PABM emulsion, a distinct Si—O—Si characteristic absorption peak is present in the range of 1000–1200 cm^{-1}. These collectively confirm the chemical composition of LPABM-*d*-LATP and the success of the polymerization. In addition, the FTIR shows a blueshift (5.6 cm^{-1}) of the symmetric stretching vibration peaks of the carboxyl group's O—C═O at 1455 and 1435 cm^{-1} in LPABM. This is because when the neutralization reaction occurs, oxygen gains more electrons from the easily ionizable lithium atoms, which leads to an increase in the electron cloud density of O—C═O.

Meanwhile, since lithiation is crucial for the ion transport properties of the polymer encapsulating layer, the effect of lithiation on its structure was investigated in detail. As is evident from the X-ray photoelectron spectra (XPS) O 1*s* spectrum in Figure 2b, the binding energy of the O 1*s* orbital decreases after neutralization (from 531.6 to 530.7 eV). This can be attributed to the fact that O completely captures the outermost electron of Li, leading to an increase in the electron cloud density of O and consequently reducing the binding energy of the electrons in the O 1*s* orbital. Moreover, as can be seen from the XPS Li 1*s* spectrum (Figure 2c), a distinct Li 1*s* peak emerged in the XPS Li 1*s* spectrum of LPABM after neutralization, signifying the successful lithiation. Additionally, to further validate the presence of lithium, we also carried out an inductively coupled plasma (ICP) test. The

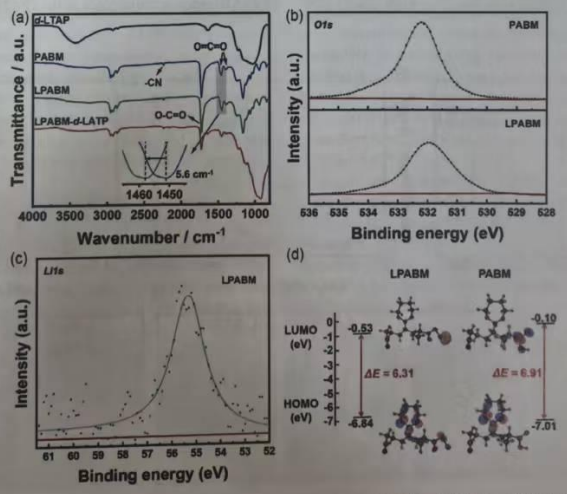

Figure 2. a) FT-IR spectra of *d*-LATP, PABM, LPABM, and LPABM-*d*-LATP. XPS b) O 1*s* spectra of PABM and LPABM, and c) L 1*s* spectra of LPABM. d) The calculated HOMO and LUMO of LPABM and PABM.

results revealed that the lithium content in PABM was less than 0.01 mg L^{-1}, whereas that in LPABM was 0.15 mg L^{-1}. This indicates that lithium is present in LPABM after lithiation.

The linear sweep voltammetry (LSV) curve is illustrated in Figure S6, Supporting Information; the operating voltage range of the battery integrated with LPABM spans from 1.2 to 3.5 V, which encompasses the working potential window of the sulfur cathode. This observation serves as evidence that LPABM maintains stability over a broad spectrum of operating voltages and is thus suitable for application in the sulfur cathode of lithium–sulfur batteries. However, owing to the partial dissolution of the PABM membrane in the electrolyte, we assembled a symmetric battery utilizing only LPABM for the LSV test. Consequently, theoretical values were also supplemented through density functional theory (DFT) calculations.[35–37] The theoretical threshold energy level of the cathode binder is computed using the following formula: $E_t = -4.5 - E_d$, where E_d represents the difference between the theoretically highest voltage of the cathode and the lowest redox potential of the lithium anode (−3.04 V vs SHE). The energy interval between the highest occupied molecular orbital (HOMO) and lowest unoccupied molecular orbital (LUMO) of the binder should encompass the working energy levels of the sulfur cathode. Otherwise, the binder will exhibit electrochemical instability within the sulfur cathode.[35,38] Consequently, the band structures of LPABM and PABM were analyzed via Gaussian DFT calculations to assess the variations in the electrochemical stability window before and after lithiation.[39] As is evident from the calculation results (Figure 2d), the HOMO and LUMO energy levels of LPABM are −6.84 and −0.53 eV, respectively, while those of PABM are −7.01 and −0.10 eV. Both sets of energy levels can encompass the working energy levels of the sulfur cathode. This finding indicates that both the LPABM and PABM binders exhibit outstanding electrochemical stability, thereby providing robust validation for the aforementioned conclusion.

Figure 3a and Figure S7, Supporting Information, show the mechanical properties of LPABM, LPABM-*d*-LATP, and LPABM/*d*-LATP. After introducing *d*-LATP to participate in copolymerization, the tensile strength of the LPABM-*d*-LATP membrane is increased from 23.6 ± 0.2 MPa of the LPABM membrane to 32.1 ± 0.2 MPa, but the elongation at break of the LPABM-*d*-LATP membrane is reduced to 191.3% ± 3.1%. This can be attributed to the fact that the double bond-modified *d*-LATP nanoparticles can be uniformly dispersed in the LPABM matrix after participating in the reaction. The nanoparticles play a reinforcing and physical cross-linking role, resulting in an increase in tensile strength and a decrease in the elongation at break of the LPABM-*d*-LATP membrane. However, the tensile strength and elongation at break of the LPABM/*d*-LATP membrane formed after solution mixing are 10.5 ± 0.3 MPa and 12.0% ± 2.9%, respectively, which are significantly lower than those of the LPABM-*d*-LATP and LPABM membranes. This is because the interaction between the LPABM and *d*-LATP is weak, and the *d*-LATP nanoparticles agglomerate and are easy to settle, resulting in defects in the LPABM/*d*-LATP membrane.

To further explore the peel strength of the LPABM, LPABM-*d*-LATP, and LPABM/*d*-LATP binders, a 180° peel test was conducted on the prepared electrode sheets. As shown in Figure 3b, the peel strength of the LPABM/*d*-LATP binder fluctuates greatly and is only 0.56 N cm^{-1}. However, the peel curve of LPABM-*d*-LATP is not only very stable but also the bonding strength is 4.93 times (2.76 N cm^{-1}) that of LPABM/*d*-LATP, but lower than the peel strength of LPABM (4.45 N cm^{-1}). This is because the introduction of *d*-LATP reduces the content of the LPABM bonding component

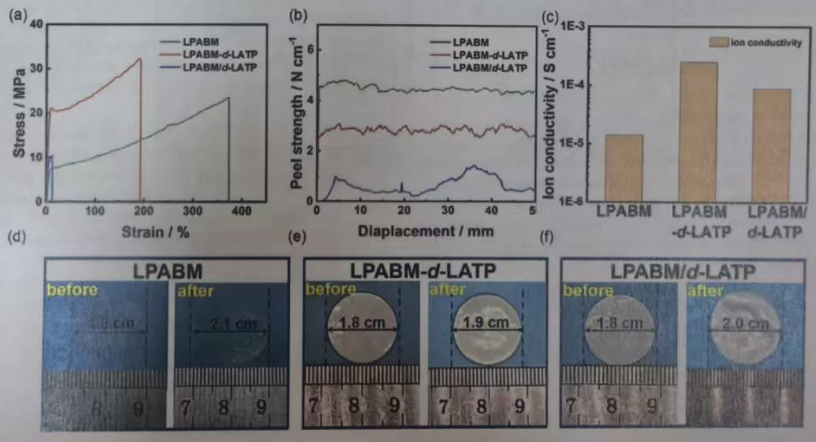

Figure 3. a) Stress–strain curves, b) peel strength, and c) ionic conductivity of LPABM, LPABM-*d*-LATP, and LPABM/*d*-LATP. d–f) Digital photos of LPABM, LPABM-*d*-LATP, and LPABM/*d*-LATP membranes before and after soaked in electrolyte for 24 h.

in the binder, resulting in a decrease in peel performance. For the LPABM/*d*-LATP binder, the *d*-LATP and LPABM components are unevenly dispersed and even agglomerate, respectively, resulting in a very poor peel strength of the LPABM/*d*-LATP binder.

We assembled three binder membranes into stainless steel symmetrical batteries to measure the ionic conductivity. As can be seen from Figure 3c, the ionic conductivity of the LPABM membrane is only 1.4×10^{-5} S cm^{-1}. The ionic conductivity of the LPABM-*d*-LATP membrane obtained after *d*-LATP participates in copolymerization is increased by more than one order of magnitude (2.5×10^{-4} S cm^{-1}). This is because the carboxylate ions in this system are more likely to combine with Ti and Al in the inorganic filler *d*-LATP, weakening the restraint of the polar carboxylate group on Li^+, reducing the migration energy barrier of Li, making the migration of Li^+ faster, resulting in a higher ionic conductivity of the LPABM-*d*-LATP membrane. However, the ionic conductivity of the LPABM/*d*-LATP membrane is lower than that of the LPABM-*d*-LATP membrane, only 8.9×10^{-5} S cm^{-1}. This is attributed to the LPABM/*d*-LATP composite binder prepared by solution mixing. The *d*-LATP agglomerates are isolated by the LPABM matrix with low ionic conductivity. *d*-LATP is limited by the Li^+ hopping of the LPABM chain, so that the high Li^+ transmission capacity of LATP cannot be fully exerted.

The electrolyte swelling resistance of LPABM, LPABM-*d*-LATP, and LPABM/*d*-LATP binders was evaluated by swelling experiments. As shown in Figure 3d–f, the LPABM binder has the worst electrolyte resistance. After immersion at room temperature, the diameter increases from 1.8 to 2.1 cm, and the electrolyte uptake of LPABM binder is 123.0%. The LPABM-*d*-LATP binder has the best electrolyte resistance. After immersion, the diameter increases from 1.8 to 1.9 cm, and the electrolyte uptake of LPABM-*d*-LATP binder is only 109.1%. The electrolyte resistance of the LPABM/*d*-LATP binder is in the middle. This is attributed to the excellent electrolyte resistance of *d*-LATP copolymerizing with LPABM to form more physical cross-linking points, thereby improving the electrolyte resistance of LPABM-*d*-LATP.

In conclusion, LPABM-*d*-LATP has better comprehensive performance than LPABM/*d*-LATP. Therefore, in this experiment, the in situ emulsion polymerization method is selected to introduce *d*-LATP into LPABM to prepare a composite ionic conductive binder.

Based on the above analysis, *d*-LATP and the degree of lithiation (corresponding to the content of MAA in the copolymer) will have a large impact on the emulsion performance, so this experiment was carried out to optimize the conditions for *d*-LATP as well as MAA dosage. First, a series of LPABM emulsions were synthesized by changing the dosages of different MAA (5%, 10%, and 15%). The mechanical property test of the emulsion membrane is shown in Figure S8a. As the dosage of MAA increases, the elongation at break of LPABM gradually decreases and the tensile strength gradually increases. This is due to the rigidity change caused by the electrostatic interaction formed between MAA and Li. Figure S8b shows the ionic conductivity of LPABM with different MAA dosages. As the dosage of MAA increases, the number of lithium ions introduced by lithiation is greatly increased, which brings a more complete lithium-ion conductive network, resulting in a continuous increase in ionic conductivity. The test results of the solvent resistance of the emulsion membrane are shown in Figure S8c, Supporting Information. LPABM-5% has the largest swelling ratio, and LPABM-15% has the smallest swelling ratio. Combining the comparison of the swelling ratios between PABM and LPABM, it can be known that as the proportion of MAA increases, the swelling ratio of LPABM decreases and is lower than the swelling ratio of the original PABM. This is attributed to the combined effect of the methyl group of MAA and the –COOLi group.

Second, a series of emulsion membranes were synthesized by changing the dosages of different *d*-LATP (3%, 5%, and 7%). Figure S9a, Supporting Information, shows the mechanical properties of the emulsion membrane. As the dosage of *d*-LATP increases, the tensile strength gradually increases while the elongation at break gradually decreases. This is because a double bond is formed between the inorganic filler *d*-LATP and the polymer, which provides a bridging structure. The structure plays a role in dispersing stress, thereby increasing the mechanical strength of emulsion membrane. However, the addition of inorganic fillers may limit the movement of polymer chains, which, in turn, leads to a decrease in the elongation at break. The results of the peel strength experiment are shown in Figure S9b. As the content of *d*-LATP increases from 3% to 7%, the peel strength decreases. This is because the inorganic filler itself has no bonding ability. As the proportion of *d*-LATP increases, the strongly adhesive LPABM part is gradually occupied by *d*-LATP without any stickiness. Therefore, peel strength continuously decreases. In addition, the ionic conductivity of the emulsion membrane is shown in Figure S9c, Supporting Information. As the content of *d*-LATP increases, the ionic conductivity of LPABM-*d*-LATP continuously increases. This indicates that the introduction of *d*-LATP not only does not affect the original Li^+ transport channel of LPABM but also has a significant enhancing effect. The test results of the solvent resistance are shown in Figure S9d. LPABM-*d*-LATP-3% has the largest swelling ratio and LPABM-*d*-LATP-7% has the smallest swelling ratio. This is because the addition of *d*-LATP may fix the connection of chemical bonds and limit the movement of molecular chains. And as the dosage of *d*-LATP increases, this limiting effect is more obvious, thereby reducing the swelling ratio of LPABM-*d*-LATP.

In summary, considering that the binder needs to take into account the mechanical properties, peel strength, ionic conductivity, and solvent resistance, the inorganic filler *d*-LATP dosage of 5% and LPABM-10% were selected as the best experimental conditions to prepare the binder in this experiment.

Figure 4a represents the mechanism of action of LPABM-*d*-LATP when used as a binder for composite sulfur cathode materials: 1) the *d*-LATP-reinforced LPABM skeleton can efficiently bind active materials with sharp volume changes; 2) the high-efficient Li^+ migration channels constructed by the interface compatibilization of *d*-LATP and –COOLi endow the sulfur cathode with rapid Li^+ migration; and 3) LPABM rich in –COOR, –COOH, –COOLi, and –CN can trap intermediate LiPS.

Figure 4b shows the 180° peeling curves of the electrode sheets prepared using different binders (LPABM, LPABM-*d*-LATP, and PVDF). As shown in Figure 4b, the peeling strength of LPABM and LPABM-*d*-LATP is significantly higher than that of

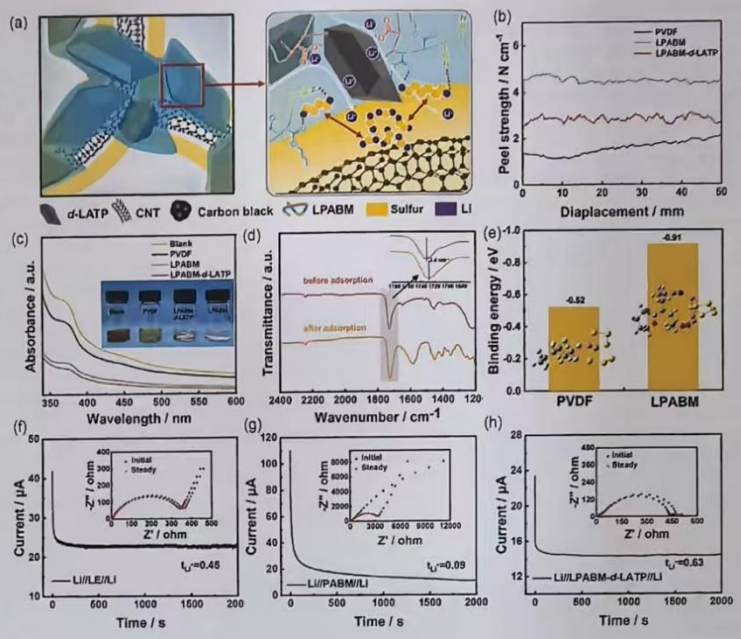

Figure 4. a) Schematic illustration for the multiple stabilization and Li^+ migration mechanisms of LPABM-*d*-LATP binder on S/CNT cathode. b) Peel strength of PVDF, LPABM, and LPABM-*d*-LATP binders. c) Digital photos of adsorbing Li_2S_6 (1 mmol L^{-1}) in DOL/DME solution and UV–vis spectra of Li_2S_6 solution after adsorption for PVDF, LPABM, and LPABM-*d*-LATP membranes. d) ATR-FTIR spectra of LPABM-*d*-LATP membrane before and after immersion in Li_2S_6 solution. e) The binding energy between LPABM, PVDF and different LiPS. EIS plots and DC polarization curves f) Li//LE//Li, g) Li//LPABM//Li, and h) Li//LPABM-*d*-LATP//Li batteries.

PVDF (1.71 N cm^{-1}). This is because the fact that the interaction between PVDF and electrode materials is mainly van der Waals force, which is relatively weak, and this weak interaction may lead to the dislodging of the electrode particles over time. In addition, the functional group –F in the PVDF binder is highly electronegative. The fluorine atoms will bind the distribution of the surrounding electron cloud, which reduces the mobility of the electrons, and the van der Waals force formed will be weakened. This leads to the low bonding performance of PVDF. In contrast, the LPABM-based binder has a higher adhesion force due to the presence of polar groups, which are able to form strong interactions with the aluminum foil.

Furthermore, to demonstrate the trapping effect of various binders on LiPS, the adsorption was observed by immersing membranes of various binders in Li_2S_6 electrolyte and quantified by UV–vis spectroscopy (Figure 4c). The absorption peak of Li_2S_6 at 370 cm^{-1} in the electrolyte of the immersed LPABM-*d*-LATP membrane was significantly attenuated, indicating that LPABM-*d*-LATP can effectively adsorb Li_2S_6. In addition, the attenuated total reflection of Fourier transform infrared spectroscopy (ATR-FTIR) of Figure 4d shows that after adsorption of LiPS, near the wave number of 1730 cm^{-1}, the $\nu_{C=O}$ peak of LPABM showed a 3.4 cm^{-1} redshift. This is because lithium ions form lithium bonds with ester groups. Lithium ions form a strong interaction with the oxygen atoms in ester groups. This interaction is mainly due to the Lewis acidic characteristic of lithium ions, which tend to form coordination bonds with the Lewis basic oxygen atoms. In this coordination process, lithium ions will attract the electron cloud on the oxygen atom, resulting in a reduction in the electron cloud density on the oxygen atom. Furthermore, DFT structural optimization and calculations indicate that taking Li_2S_6 as an example, the calculated binding energy with LPABM-*d*-LATP is −0.91 eV, which is much stronger than the binding energy with PVDF (−0.52 eV) (Figure 4e). This shows that LiPS species tend to approach the ester groups, carboxyl groups, and cyano groups in the LPABM-based binder.

The lithium-ion transference number (t_{Li^+}) is also very important to evaluate the performance of ionic conductive binders. Therefore, Li//LE//Li, Li//PABM//Li, and Li//LPABM-*d*-LATP//Li symmetrical batteries were assembled and subjected to polarization tests with an initial voltage of 10 mV for 2000 s and electrochemical impedance spectroscopy (EIS) tests before and after

polarization, as shown in Figure 4f–h. According to the obtained alternating current impedance and direct current polarization data, and through the Bruce–Vicent equation, the lithium-ion transfer number (t_{Li^+}) of different substances can be calculated. Therefore, it is calculated that the t_{Li^+} of LPABM-*d*-LATP is as high as 0.63, while those of LPABM and the electrolyte are 0.09 and 0.45, respectively. This is because the synergistic effect of *d*-LATP and –COOLi constructs a dual lithium-ion conductive channel, endowing the sulfur cathode with rapid t_{Li^+} migration, thereby increasing the migration number of lithium ions.

In addition, LPABM-*d*-LATP has good adhesion and mechanical strength, which can maintain the integrity of the electrode structure and reduce the impact of volume changes during the charging and discharging process on the electrode structure, thereby facilitating the migration of lithium ions. This is also a property that ordinary commercial PVDF binders do not have when used in LSBs. The above experiments demonstrated the dual lithium-ion migration mode, namely, the synergistic effect between the LPABM chain segments as well as the LATP, can promote ion migration.

In order to verify the effectiveness of LPABM-*d*-LATP in augmenting the electrochemical reaction kinetics of sulfur cathode, lithium–sulfur batteries are further assembled with S/CNT cathodes of various binders and lithium sheets to investigate electrochemical performance. The cyclic voltammetry (CV) curves of each battery at an identical scanning rate of 0.2 mV s^{-1} are compared in **Figure 5a**. In the CV curves, typical oxidation and reduction peaks characteristic of a lithium–sulfur battery (LSB) are observed. All CV curves invariably presented an oxidation peak (P_A) and two clear reduction peaks ($P_C{}^1$ and $P_C{}^2$). Specifically, the conversion of $Li_2S_2/Li_2S \rightarrow S_8$ occurs at the oxidation peak within the voltage range of 2.3–2.4 V. Meanwhile, the series of reactions $S_8{}^{2-} \rightarrow S_6{}^{2-} \rightarrow S_4{}^{2-}$ take place at the reduction peak in the 2.3–2.4 V interval.[40] At the reduction peak ranging from 2.0 to 2.1 V, the transformation $S_4{}^{2-} \rightarrow S_2{}^{2-} \rightarrow Li_2S$ is observed. LPABM-*d*-LATP displays more distinct oxidation peaks in the CV curve. This phenomenon can be ascribed to its higher lithium-ion conductivity, which accelerates the transport of lithium ions and facilitates the conversion of lithium polysulfides. Additionaliy, based on the voltage values corresponding to the oxidation and reduction peaks (Figure 5b), the polarization voltage of LPABM-*d*-LATP is determined to be 0.285 V. This value is lower than that of LPABM (0.412 V) and PVDF (0.481 V), thereby indicating that LPABM-*d*-LATP possesses superior reversibility.

The CV test describes the detailed redox reactions and electrochemical kinetics of the battery during charging and discharging. The above study demonstrated that the LPABM-*d*-LATP binder has a positive effect on the electrochemical reaction kinetics of LSBs, therefore carried out further CV tests. Figure S10, Supporting Information, shows typical CV curves for LPABM, PVDF, and LPABM-*d*-LATP at six different scan rates. Unlike the CV curves of PVDF and LPABM, which have only one observable oxidation peak, the cathode of LPABM-*d*-LATP shows two oxidation peaks at about 2.3 and 2.4 V, respectively. This may be because LPABM adequately encapsulates the active material but has limited ionic conduction, resulting in a high degree of polarization. Therefore, only one oxidation peak appears at 2.45 V. And for PVDF, the oxidation peak shows an overlap of peaks at 2.36 and 2.46 V, and the peak width is relatively large, indicating that its reaction kinetics is slow. In contrast, LPABM-*d*-LATP exhibits superior ionic conductivity, which accelerates the transport of lithium ions. The lower polarization voltage of battery with LPABM-*d*-LATP, compared to both LPABM and PVDF, indicates more favorable reaction kinetics. Moreover, its higher lithium-ion conductivity facilitates the complete conversion of sulfur species and thereby may enhance the reversibility of the

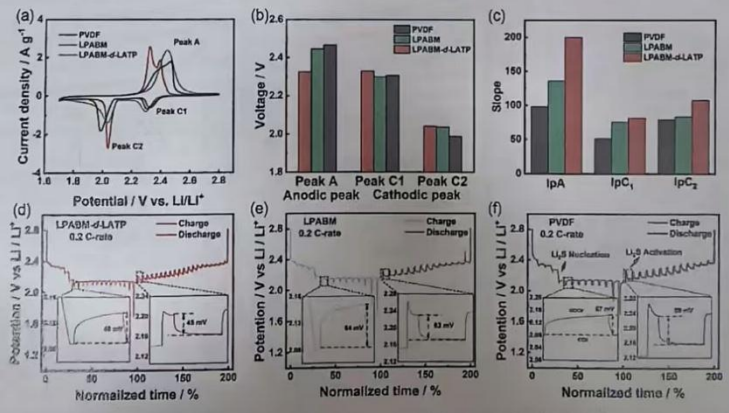

Figure 5. a) CV curves at a scan rate of 0.2 mV s^{-1}, b) oxidation and reduction peaks, and c) corresponding linear fitting slopes between peak current and square root rate of Peek A, C1, and C2 for Li-S batteries with different binders. GITT curves for Li–S batteries with d) LPABM-*d*-LATP, e) LPABM, and f) PVDF binders.

electrochemical process. These results imply that the LPABM-*d*-LATP sulfur cathode has better reversibility and faster electrode kinetics, which will improve electrochemical performance. Figure 5c and Figure S11, Supporting Information, show the results of the linear fitting of the corresponding peak currents against the square root of the scanning rate at diverse scanning rates, wherein the slope of the fitting curve is positively correlated with the lithium-ion diffusion rate. The calculated slope of LPABM-*d*-LATP is larger than that of LPABM, signifying a more rapid lithium-ion diffusion. Finally, the Li^+ diffusion coefficients (D_A, D_C^1, and D_C^2) were calculated through Randles–Sevcik equation.[41] The lithium-ion diffusion coefficients of the LPABM-*d*-LATP-based cathodes were D_A ($2.82 \times 10^{-7} cm^2 s^{-1}$), D_C^1 ($5.65 \times 10^{-8} cm^2 s^{-1}$), and D_C^2 ($8.25 \times 10^{-8} cm^2 s^{-1}$), all of which are superior to those based on the PVDF and LPABM cathodes (Table S1, Supporting Information). It is demonstrated that the employment of the LPABM-*d*-LATP binder system fortifies the lithiation/delithiation kinetics of the sulfur cathode. This enhancement can be ascribed to the dual Li^+ channel transmission mode formed by –COOLi on copolymer chains and uniform LATP particles in LPABM-*d*-LATP binder, enhanced Li^+ diffusion.

Galvanostatic intermittent titration technique (GITT) analyzes the electrochemical characteristics of battery materials by applying a constant current pulse, which can provide detailed information regarding the electrochemical behavior of electrode materials during the charging and discharging processes. Through the analysis of the variation of potential over time, valuable kinetic information within the battery can be obtained.[42,43] Consequently, GITT is used to investigate the charge transfer capability of batteries with different binders during the charging/discharging process at a current density of 0.2 C (Figure 5d–f). It is evidently seen that the ΔIR (49 m V for Li_2S nucleation and 45 m V for Li_2S activation) of the battery with LPABM-*d*-LATP during solid–liquid transformation is lower than that of LPABM (64 and 62 m V) and PVDF (67 and 89 m V). This implies that the LPABM-*d*-LATP-based battery exhibits the minimum polarization and a relatively small internal resistance during the discharge process, thereby facilitating the nucleation and oxidation of Li_2S. This is because a higher ion transport capability can effectively reduce polarization during the battery cycling process.

The electrochemical performance of LPABM-*d*-LATP-based batteries was further explored. Galvanostatic charge–discharge (GCD) analysis was performed for lithium–sulfur batteries with different binders at a current density of 0.1 C. As can be seen in **Figure 6a**, the specific capacities of LPABM-*d*-LATP-, LPABM-, and PVDF-based batteries are 1204, 1019, and 928 m Ah g^{-1}, respectively. Moreover, compared to batteries with LPABM (172 m V) and PVDF (184 m V), the battery with LPABM-*d*-LATP exhibited a relatively lower overpotential of 163 m V. These two aspects jointly suggest that augmenting the ion transport capability within the sulfur cathode can effectively diminish polarization and enhance the utilization efficiency of the active materials. Figure 6b presents the rate performance of batteries with three types of binders over the current density range of 0.1, 0.2, 0.5, 1, 2, 3, and 4 C. The LPABM-*d*-LATP-based battery consistently maintains the highest specific capacity (915 m Ah g^{-1} at 4 C, in contrast to 713 and 217 m Ah g^{-1} for LPABM and PVDF, respectively), which is comparable to the levels of some recently reported works (Table S2, Supporting Information). Thereby, it is

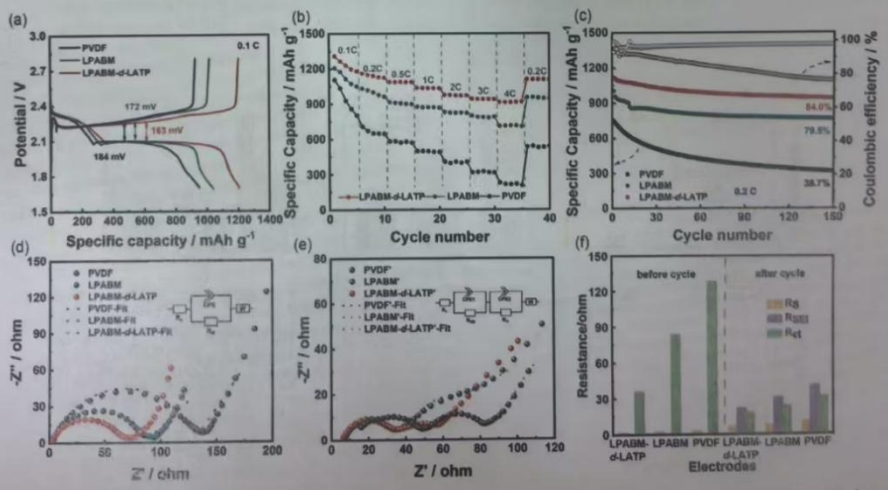

Figure 6. a) Galvanostatic charge/discharge curves at 0.1 C, b) rate performance, and c) cycling performance of Li–S batteries based on different binders at 0.2 C. d) Nyquist plots before cyclic test, e) Nyquist plots after cyclic test, and f) impedance corresponding to equivalent circuit simulation before and after cycling for Li–S batteries based on different binders.

demonstrated that LPABM-*d*-LATP binder can significantly promote the reaction kinetics of the batteries.

Regarding the cycle stability of different binders (Figure 6c), after 150 cycles at 0.2 C, the discharge specific capacity of the sulfur cathode based on LPABM-*d*-LATP is 941 m Ah g^{-1}, with an average capacity decay of only 0.107% per cycle. In contrast, the capacity of sulfur cathodes based on LPABM and PVDF was 765 m Ah g^{-1} (0.137% capacity decay per cycle) and 292 m Ah g^{-1} (0.307% capacity decay per cycle), respectively. Concurrently, as depicted in Figure S13, Supporting Information, the capacity retention ratio of the LSB based on the LPABM-*d*-LATP binder was 80.1% after 200 cycles at 0.5 C. Additionally, the cycling stability of LSBs with LPABM-*d*-LATP under high sulfur loading (4.7 mg cm^{-2}) was also evaluated. At a current density of 0.2 C, the specific capacity of the LPABM-*d*-LATP-based battery reached as high as 983 m Ah g^{-1}, and the retention ratio after 100 cycles was 83.1%, which was substantially superior to that of the LSB based on PVDF (Figure S14, Supporting Information).

Subsequently, EIS test was utilized to further reveal the interfacial electrochemical properties of batteries based on three different binders. As shown in Figure 6d,e and Table S3, Supporting Information, regardless of before and after cycling, the impedance value of LPABM-*d*-LATP was the lowest (75 Ω before cycling, 60 Ω after cycling), followed by LPABM (95 Ω before cycling, 70 Ω after cycling) and the largest for PVDF (140 Ω before cycling, 85 Ω after cycling). This was attributed to the fact that LPABM-*d*-LATP binder furnished a uniform structure and a complete conductive network. Through the fitting of the EIS data before and after cycling (Figure 6f), the equivalent series resistance (R_s) and charge transfer resistance (R_{ct}) of PVDF prior to cycling were 2.7 Ω and 127.8 Ω, respectively. In comparison, the R_s and R_{ct} of fresh batteries with LPABM-*d*-LATP and LPABM were 1.5, 35.5 Ω and 1.9, 83.2 Ω, respectively, which were evidently smaller. This indicates that the LPABM-*d*-LATP binder possessed a more efficient ion conductive network and more rapid ion transport rate. After the cycling test, it was observed that the R_{ct} of all three types of batteries decreased, which could be attributed to the dispersion effect of the active materials resulting from repeated charging and discharging. Moreover, in the EIS spectra of these batteries after cycling, an additional semicircle was observed. This semicircle corresponds to the impedance of the solid electrolyte interface (SEI) layer formed on the anode (R_{SEI}). The R_{SEI} value for the battery incorporating LPABM-*d*-LATP was merely 21.29 Ω, signifying that a relatively small amount of lithium polysulfides (LiPS) shuttled to the anode, thereby contributing to the stability of the SEI layer. In contrast, the R_{SEI} value for the PVDF-based battery was 40.70 Ω, which is approximately double that of the LPABM-*d*-LATP-based battery. This indicates that PVDF exhibits a relatively weak capability in suppressing the shuttling of LiPS.

Finally, in order to further compare the ability of different binders to maintain the integrity of the bonding structure after long cycles, the SEM images of the electrodes with different binders before and after 50 cycles were observed (Figure S15, Supporting Information). The electrodes of the batteries with LPABM-*d*-LATP showed a relatively lower density of cracks on the electrode surface even after prolonged cycling, which could be ascribed to its favorable mechanical properties and high adhesion characteristics. Conversely, obvious cracks (≈10 μm in width) appeared on the surface of the sulfur cathode with PVDF after cycling. Owing to the lack of elasticity of the PVDF itself which made it difficult to inhibit the volumetric deformation of the sulfur cathode. This indicates that LPABM-*d*-LATP has a better ability to maintain the structural integrity of the battery than PVDF.

3. Conclusion

The reactive functionalized lithium titanium aluminum phosphate was obtained by surface modification of LATP with silane coupling agent to introduce vinyl group. Then the ionic conductive binder (LPABM-*d*-LATP) based on interface compatibilization of fast ionic conductors with BA, AN, MAA, and *d*-LATP as monomers was obtained by in situ emulsion polymerization and neutralization treatment. By investigating the effects of the introduction and amount of MAA and *d*-LATP monomers, as well as the effects on the structure and properties of the binder before and after lithiation, the best overall performance of LPABM-*d*-LATP was obtained when the ratio of monomers was AN:BA:MAA:LATP = 10:7:2:1 and polymers were lithiated. Lithium–sulfur batteries with typical sulfur loading (2.0 mg cm^{-2}) using LPABM-*d*-LATP binder had an initial specific capacity of 1204 m Ah g^{-1} at 0.1 C and maintained a specific capacity of 941 m Ah g^{-1} at a high rate of 4 C. The results also showed that the LPABM-*d*-LATP-based batteries had 80.1% capacity retention after 200 cycles of the 0.5 C cycling test. This work provides a new binder system suitable for sulfur cathodes, which is potentially valuable for large-scale production applications.

4. Experimental Section

Synthesis of LATP Nanoparticles Modified with Double Bonds

Two grams of $Li_{1.3}Al_{0.3}Ti_{1.7}(PO_4)_3$ (LATP) nanoparticles were ultrasonically dispersed in 50 mL of ethanol and transferred to a three-necked flask equipped with a stirring paddle and a thermometer. Then 80 mg of chloro(dimethyl)vinylsilane coupling agent and 1 mL of deionized water were added dropwise and stirred for 24 h at 50 °C; the product was washed with ethanol for several times and then dried in a vacuum at 60 °C for 24 h to obtain the LATP nanoparticles modified with double bonds (*d*-LATP).

Synthesis of LPABM Binders

BA, AN, and MAA were added in a certain proportion to deionized water containing divinylbenzene (DVB) cross-linking agent and sodium nonylphenol ethoxylate sulfate emulsifier. The above mixture is emulsified into a stable emulsion through a high-speed homogenizer. The pre-emulsion is transferred to a four-necked round bottom flask equipped with a thermometer and a mechanical stirrer, and the argon is pumped to remove dissolved oxygen. Afterward, the aqueous solution composed of ammonium persulfate (APS) and sodium bisulfite ($NaHSO_3$) was added dropwise and further reacted for 5 h at 50 °C to obtain the PABM emulsion. Then, a certain amount of 1 mol L^{-1} aqueous LiOH solution is dropped into PABM for lithiation

neutralization to obtain LPABM binder. A series of PABM and LPABM with different components are prepared by adjusting the amount of MAA (Table S4, Supporting Information).

Synthesis of LPABM-*d*-LATP Binders

The ionic conductive binder based on the interface compatibilization of fast ionic conductor (LPABM-*d*-LATP) is obtained by in situ emulsion polymerization and lithiation neutralization. The specific steps are as follows: a certain amount of *d*-LATP, BA, AN, MAA, sodium nonylphenol ethoxylate sulfate, and DVB were added to deionized water. The above mixture is emulsified into a stable emulsion through a high-speed homogenizer. The pre-emulsion is transferred to a four-necked round bottom flask equipped with a thermometer and a mechanical stirrer, and argon is pumped to remove dissolved oxygen. Afterward, the aqueous solution composed of APS and $NaHSO_3$ was added dropwise and further reacted for 5 h at 50 °C to obtain the PABM-*d*-LATP precursor emulsion. Then, a certain amount of 1 mol L^{-1} aqueous LiOH solution is dropped into to PABM-*d*-LATP for lithiation neutralization to obtain LPABM-*d*-LATP binder. A series of LPABM-*d*-LATP with different components were prepared by adjusting the dosage of *d*-LATP (Table S5, Supporting Information).

Synthesis of LPABM/d-LATP Co-Binders

The *d*-LATP powder was mixed into the LPABM emulsion at a ratio of 5% and deionized water was added to obtain the LPABM/*d*-LATP co-binders with a solid content of 5 wt%.

Preparation of Sulfur Cathodes and Assembly of Batteries

The S/CNT composite (S:CNT = 3:1) is obtained by ball milling at 200 rpm for 6 h and melting in an argon atmosphere at 155 °C for 12 h. The cathode slurry is prepared by ball milling the S/CNT composite, carbon black, and binder in a mass ratio of 8:1:1 for 6 h. And the solid content of slurry is controlled to ≈30 wt%. After the obtained slurry is coated on aluminum foil by using an applicator with a gap of 200 μm and dried naturally, it is put into vacuum oven for 12 h at 60 °C to thoroughly dry. The typical mass loading of cathode is ≈2.4 mg cm^{-2}. In addition, for higher sulfur loading, the cathode is prepared by coating a thicker slurry (the solid content of ≈40 wt%) on a carbon-coated aluminum foil with an applicator (the gap is 400 μm). The mass loading of this cathode is ≈5.2 mg cm^{-2}.

Coin-type (CR2016) batteries were assembled in an argon-filled glove box. The sulfur cathode is separated from the mental lithium anode with polypropylene separator (Celgard 2400). The electrolyte consisted of 1 M lithium bis-(trifluoromethylsulfonyl) imide (LiTFSI) in the mixture of 1,2-dimethoxyethane and 1,3-dioxolane (1/1, V/V) containing $LiNO_3$ (1 wt%). The amount of electrolyte is determined by the mass of sulfur, which is 20 μL mg^{-1}.

Characterization

The morphologies of the samples are characterized by field-emission SEM (FE-SEM, Hitachi S4800) and TEM (JEOL JEM-F200). FTIR analyses are conducted on Nicolet 6700. UV–vis spectroscopy tests are conducted on Shimadzu UV-2450. The XPS analysis is conducted on Thermo Scientific ESCALAB Xi+. The ICP analysis is conducted on Agilent 5800ICP-OES. The mechanical properties are carried out at a strain rate of 13 mm min^{-1} via a high precision dynamometer (M7, Mark-10). Peel strength test using Mark-10 ESM303 tensile testing machine for 180° peel test. Ionic conductivity was tested using Shanghai Chenhua CHI760E electrochemical workstation. Contact angle is tested using Shanghai Zhongchen JC2000D2 contact angle measuring instrument.

Electrochemical Measurements

All electrochemical measurements were conducted in a 25 °C incubator. And the EIS measurements, the CV, and the LSV measurements were carried out on the electrochemical workstation (CHI760e). Besides, constant current charging/discharging (GCD) tests, GITT, and cycle stability tests were performed on the battery test system (NEWARE, Shenzhen, China). The voltage windows for GCD and CV tests were between 1.8 and 2.7 V. For a current density of 0.5 C, the cells were activated one cycle in advance at 0.1 C. EIS tests were conducted in the frequency range of 1–10 MHz and the test amplitude was 5 mV.

Theoretical Calculation

We conducted geometrical optimizations and calculations based on the M06-2X/6-311+g (d) basis set for all configurations involved in the energy levels, the transition states, and the reaction pathways. And the implicit solvent was chosen as 1,4-dioxane, which was similar to 1,3-dioxane. Subsequently, geometrical optimizations were conducted on the optimized structures by DFT-D3 dispersion correction in the gas phase. Then, frequency calculations were conducted on the optimized structure to ensure that it was at the local minimum of the potential energy surface. The solvation Gibbs free energy was obtained at the theoretical level of M06 2X/6-311+g (d) by the cluster-continuum solvation method, which used the implicit solvent model and Gibbs free energy correction at $P = 1$ atm and $T = 298.15$ K. We also calculated the LUMO and HOMO energy levels of the binder molecule.

Acknowledgements

L.D. and X.F. contributed equally to this work. The authors greatly appreciate the financial supports of National Natural Science Foundation of China (grant nos. 22478120 and 22109045).

Conflict of Interest

The authors declare no conflict of interest.

Data Availability Statement

The data that support the findings of this study are available from the corresponding author upon reasonable request.

Keywords: conductive binders · emulsion polymerization · fast ionic conductor · lithium–sulfur batteries · sulfur cathodes

[1] R. F. Service, *Science* **2018**, *359*, 1080.
[2] V. Viswanathan, A. H. Epstein, Y.-M. Chiang, E. Takeuchi, M. Bradley, J. Langford, M. Winter, *Nature* **2022**, *601*, 519.
[3] P. Su-ungkavatin, L. Tiruta-Barna, L. Hamelin, *Prog. Energy Combust. Sci.* **2023**, *96*, 101073.
[4] J. Chen, G. Liu, X. Han, H. Wu, T. Hu, Y. Huang, S. Zhang, Y. Wang, Z. Shi, Y. Zhang, L. Shi, Y. Ma, H. N. Alshareef, J. Zhao, *ACS Nano* 2024, *18*, 13662.
[5] J. Chen, J. Zhao, L. Lei, P. Li, J. Chen, Y. Zhang, Y. Wang, Y. Ma, D. Wang, *Nano Lett.* **2020**, *20*, 3403.
[6] S. Li, J. Chen, G. Liu, H. Wu, H. Chen, M. Li, L. Shi, Y. Wang, Y. Ma, J. Zhao, *ACS Appl. Mater. Interfaces* **2022**, *14*, 56697.

[7] S. Zhou, J. Shi, S. Liu, G. Li, F. Pei, Y. Chen, J. Deng, Q. Zheng, J. Li, C. Zhao, I. Hwang, C.-J. Sun, Y. Liu, Y. Deng, L. Huang, Y. Qiao, G.-L. Xu, J.-F. Chen, K. Amine, S.-G. Sun, H.-G. Liao, *Nature* **2023**, *621*, 75.
[8] Y. Zhong, Q. Wang, S.-M. Bak, S. Hwang, Y. Du, H. Wang, *J. Am. Chem. Soc.* **2023**, *145*, 7390.
[9] S. C. Kim, X. Gao, S.-L. Liao, H. Su, Y. Chen, W. Zhang, L. C. Greenburg, J.-A. Pan, X. Zheng, Y. Ye, M. S. Kim, P. Sayavong, A. Brest, J. Qin, Z. Bao, Y. Cui, *Nat. Commun.* **2024**, *15*, 1268.
[10] J. Liu, Y. Zhou, T. Yan, X.-P. Gao, *Adv. Funct. Mater.* **2024**, *34*, 2309625.
[11] Q. Shao, S. Zhu, J. Chen, *Nano Research* **2023**, *16*, 8097.
[12] K. Kakiage, T. Yano, H. Uehara, M. Kakiage, *Commun. Eng.* **2024**, *3*, 177.
[13] D. M. Brieske, A. Warnecke, D. U. Sauer, *Energy Storage Mater.* **2023**, *55*, 289.
[14] M. Yamamoto, S. Goto, R. Tang, K. Nomura, Y. Hayasaka, Y. Yoshioka, M. Ito, M. Morooka, H. Nishihara, T. Kyotani, *ACS Appl. Mater. Interfaces* **2021**, *13*, 38613.
[15] Z. Han, H.-R. Ren, Z. Huang, Y. Zhang, S. Gu, C. Zhang, W. Liu, J. Yang, G. Zhou, Q.-H. Yang, W. Lv, *ACS Nano* **2023**, *17*, 4453.
[16] J. Li, L. Gao, F. Pan, C. Gong, L. Sun, H. Gao, J. Zhang, Y. Zhao, G. Wang, H. Liu, *Nano-Micro Lett.* **2023**, *16*, 12.
[17] S. Feng, Z.-H. Fu, X. Chen, Q. Zhang, *InfoMat* **2022**, *4*, e12304.
[18] W. Jin, X. Zhang, M. Liu, Y. Zhao, P. Zhang, *Energy Storage Mater.* **2024**, *67*, 103223.
[19] Z. Pan, D. J. L. Brett, G. He, I. P. Parkin, *Adv. Energy Mater.* **2022**, *12*, 2103483.
[20] T. Ma, J. Deng, Y. Lin, Q. Liang, L. Hu, X. Wang, J. Liu, X. Zhao, Y. Li, D. Nan, X. Yu, *Energy Environ. Mater.* **2024**, *7*, e12704.
[21] F. Pei, L. Wu, Y. Zhang, Y. Liao, Q. Kang, Y. Han, H. Zhang, Y. Shen, H. Xu, Z. Li, Y. Huang, *Nat. Commun.* **2024**, *15*, 351.
[22] Z. Shi, Z. Tian, D. Guo, Y. Wang, Z. Bayhan, A. S. Alzahrani, H. N. Alshareef, *ACS Energy Lett.* **2023**, *8*, 3054.
[23] S. Bai, X. Liu, K. Zhu, S. Wu, H. Zhou, *Nat. Energy* **2016**, *1*, 16094.
[24] J. Pu, T. Wang, Y. Tan, S. Fan, P. Xue, *Small* **2023**, *19*, 2303266.
[25] Y. Wu, M. Yang, Y. Zou, S. Hou, B. Hu, S. Wang, Y. Tao, C. Yang, *New J. Chem.* **2022**, *46*, 20129.
[26] H. Wang, Y. Wang, G. Zhang, Z. Yang, Y. Chen, Y. Deng, Y. Yang, C. Wang, *Electrochim. Acta* **2021**, *371*, 137822.
[27] X. Luo, X. Lu, X. Chen, Y. Chen, C. Yu, D. Su, G. Wang, L. Cui, *J. Energy Chem.* **2020**, *50*, 63.
[28] Q. Qi, X. Lv, W. Lv, Q.-H. Yang, *J. Energy Chem.* **2019**, *39*, 88.
[29] J. Liu, Q. Zhang, Y.-K. Sun, *J. Power Sources* **2018**, *396*, 19.
[30] V. Singh, A. K. Padhan, S. D. Adhikary, A. Tiwari, D. Mandal, T. C. Nagaiah, *J. Mater. Chem. A* **2019**, *7*, 3018.
[31] M. Si, X. Jian, Y. Xie, J. Zhou, W. Jian, J. Lin, Y. Luo, J. Hu, Y.-J. Wang, D. Zhang, T. Wang, Y. Liu, Z. L. Wu, S. Y. Zheng, J. Yang, *Adv. Energy Mater.* **2024**, *14*, 2303991.
[32] L. Cheng, R. Tian, Y. Zhao, Z. Wei, X. Pu, Y.-L. Zhu, D. Zhang, F. Du, *Nano Lett.* **2023**, *23*, 10538.
[33] W. Wang, L. Hua, Y. Zhang, G. Wang, C. Li, *Angew. Chem. Int. Ed.* **2024**, *63*, e202405920.
[34] X. Lin, X. Liu, Y. Tong, X. Zhou, J. Li, J. Song, X. Feng, R. Liu, L. Shi, A. Yu, Y. Ma, *Adv. Funct. Mater.* **2024**, *34*, 2406985.
[35] W. Chen, T. Lei, T. Qian, W. Lv, W. He, C. Wu, X. Liu, J. Liu, B. Chen, C. Yan, J. Xiong, *Adv. Energy Mater.* **2018**, *8*, 1702889.
[36] L. Yuan, X. Qiu, L. Chen, W. Zhu, *J. Power Sources* **2009**, *189*, 127.
[37] J. Wang, Z. Yao, C. W. Monroe, J. Yang, Y. Null, *Adv. Funct. Mater.* **2013**, *23*, 1194.
[38] L. Yuan, X. Qiu, L. Chen, W. Zhu, *J. Power Sources* **2009**, *189*, 127.
[39] W. Chen, T. Qian, J. Xiong, N. Xu, X. Liu, J. Liu, J. Zhou, X. Shen, T. Yang, Y. Chen, C. Yan, *Adv.Mater* **2017**, *29*, 1605160.
[40] X. Sun, Y. Qiu, B. Jiang, Z. Chen, C. Zhao, H. Zhou, L. Yang, L. Fan, Y. Zhang, N. Zhang, *Nat. Commun.* **2023**, *14*, 291.
[41] C.-L. Yang, L.-N. Wang, P. Yin, J. Liu, M.-X. Chen, Q.-Q. Yan, Z.-S. Wang, S.-L. Xu, S.-Q. Chu, C. Cui, H. Ju, J. Zhu, Y. Lin, J. Shui, H.-W. Liang, *Science* **2021**, *374*, 459.
[42] D. W. Dees, S. Kawauchi, D. P. Abraham, J. Prakash, *J. Power Sources* **2009**, *189*, 263.
[43] M. Jia, W. Zhang, X. Cai, X. Zhan, L. Hou, C. Yuan, Z. Guo, *J. Power Sources* **2022**, *543*, 231843.

Manuscript received: December 22, 2024
Revised manuscript received: April 23, 2025
Version of record online: June 29, 2025